Quantifying Global-Warming Response of the Orographic Precipitation in a Typhoon Environment with Large-Eddy Simulations

Jianan Chen[a] and Xiaoming Shi[a]

[a] *Division of Environment and Sustainability, Hong Kong University of Science and Technology, Hong Kong, China*

Corresponding author: Jianan Chen, jianan.chen@connect.ust.hk

Preprint statement

This manuscript is non-peer reviewed preprint and has been submitted to Journal of Climate for peer review.

Quantifying Global-Warming Response of the Orographic Precipitation in a Typhoon Environment with Large-Eddy Simulations

Jianan Chen[a] and Xiaoming Shi[a]

[a] *Division of Environment and Sustainability, Hong Kong University of Science and Technology, Hong Kong, China*

Corresponding author: Xiaoming Shi, shixm@ust.hk

ABSTRACT

The intense and moist winds in a tropical cyclone (TC) environment can produce strong mountain waves and substantially enhanced precipitation over complex terrain, yet few studies investigated how the orographic precipitation in a TC environment might respond to global warming. Here, we use large-eddy simulation to estimate the global warming-induced change in the precipitation over and near an idealized mountain with pseudo-global warming experiments. Two regions in the simulations exhibit locally enhanced precipitation, one over the mountain and the other in the downstream region 25 to 45 km away from the mountain. The enhanced precipitation in both regions is related to the seeder-feeder mechanism, though the enhancement in the downstream regions differs from the conventional definition and is referred as pseudo-seeder-feeder mechanism (PSF). In the PSF mechanism, mountain waves generate an intense cloud formation center in the mid-troposphere above the lee slope, and the resulting precipitation particles drift downstream, intensifying downstream convection when they fall into proper locations and heights. Under warming, the precipitation maximum over the mountain exhibits minimal change, while the precipitation maximum in the downstream region exhibiting sensitivity of around 18 % K^{-1} intensifies and shifts towards the mountain. The small sensitivity of the first precipitation peak is due to the canceling effects of thermodynamic and dynamic changes. The large sensitivity in the downstream region is mainly due to the strengthening of the wave-induced mid-troposphere cloud formation center which supplies more hydrometeors to the downstream region and enhances precipitation efficiency through the enhanced PSF mechanism.

SIGNIFICANCE STATEMENT

The combination of typhoon environment and orography can produce intense precipitation and thereby severe flooding risks. Here, we investigate the global-warming response of orographic precipitation in a typhoon environment with idealized, high-resolution simulations. The experiments suggest that under warming, a precipitation maximum may emerge in the downstream region of a mountain, or strengthen and shift upwind if it already exists in the current climate. This surprising amplification of downstream region precipitation is related to the enhancement of the mid-tropospheric cloud generation caused by mountain waves and has critical implications to flooding risk management in mountainous regions.

1. Introduction

The mountains and their foothills are dwelling places for around 26% of the global population (Beniston 2005). An essential source of water supply in the mountainous region is orographic precipitation (Schär and Frei 2005). Yet, heavy orographic precipitation can also induce flash floods and subsequently bring social and economic damages to human society (Houze 2012). It's therefore of critical importance to assess how the orographic precipitation will change in response to the warming climate.

Global warming can affect orographic precipitation through modification of thermodynamic, dynamic, and cloud microphysics factors. Under global warming, with roughly unchanged relative humidity, the water vapor in the atmosphere will increase by ~7% K^{-1} of surface warming based on the Clausius–Clapeyron (CC) equation (O'Gorman 2015). The increased moisture in a warmed climate is expected to increase precipitation over mountains. For example, Jing et al. (2019) show that in their pseudo-global warming simulations, the projected increase of wintertime precipitation in the interior western United States mountains under global warming is mainly induced by increased moisture with other factors playing secondary roles. Nonetheless, the increased temperature and moisture can alter the gravity wave dynamics which can further affect the precipitation. Shi and Durran (2015) conducted an idealized study to investigate the orographic precipitation over idealized north-south oriented midlatitude mountain barriers and found the extreme precipitation over the eastern slope increases at a rate higher than that over the western slope. The relatively strong response over the eastern slope is explained by the vertical velocity change which is governed by gravity wave dynamics. The change in atmospheric stability and cross-mountain wind speed is critical because they determine whether the incoming airstream is blocked by the mountain of interest (Eidhammer et al. 2018; Kirshbaum et al. 2018). In the blocked case, the incoming airstream tends to deflect around the mountain instead of passing over it (Kirshbaum et al., 2018); without substantial forced lifting, heavy precipitation is less likely to occur. Large-scale circulation shifts under warming can affect where the precipitation forms through the moisture transport (Shi and Durran, 2014). The warming response of microphysical processes occurring in clouds has been investigated in several studies (Kirshbaum et al. 2018). Kirshbaum and Smith (2008) found that precipitation efficiency (PE) will decrease in response to warming because the mixed-phase rain processes are partly replaced by the less efficient warm rain process. Pavelsky et al. (2012) show that the lifted freezing level in a warmed climate may cause an upwind shift of orographic distribution. With a higher freezing level, falling hydrometeors from upper levels will shift from solid phase to liquid phase earlier. Considering the faster falling speed of liquid hydrometeors, the hydrometeors will fall in a shorter distance and therefore cause an upwind shift in the precipitation distribution (Pavelsky et al. 2012).

Some of the most intense precipitation events happen when tropical cyclones (TCs) pass over complex terrain (Houze 2012; Smith et al. 2009). A TC can produce heavy rainfall directly in its spiral rainband and eyewall, or indirectly through the interaction between its circulation with mountain ranges (Wang et al. 2009). When a steep mountain range intersects with TC circulation, the environmental conditions featuring strong surface wind, moist air, and low static stability are consistent with empirical conditions favoring the occurrence of intense orographic precipitation (Lin et al. 1998). However, previous research has not investigated how the orographic precipitation induced by the interaction between mountain range and TC outer region circulation will change in response to warming. This might be due to two reasons. Firstly, it is computationally infeasible to simulate a TC spanning thousands of kilometers horizontally with large-eddy simulation (LES) resolution that can explicitly resolve the fine-scale process (Bryan et al. 2017). The use of convection parameterization is often accused of being the reason for inconsistent prediction of extreme precipitation sensitivities to warming in climate models (Muller, 2013; O'Gorman, 2015). To avoid the uncertainties brought by the convection parameterization schemes, convection-permitting models with horizontal grid spacings on the order of one kilometer have been employed to investigate the warming response of convective systems (Guichard and Couvreux 2017; Kirshbaum and Smith 2008). However, the kilometer-scale resolution is in the gray zone of convection and terrain (for smaller mountains) and how to resolve gray zone issues is an ongoing topic (Chow et al. 2019). LES can help avoid those uncertain issues, but it is computationally demanding to conduct three-dimensional typhoon simulations at the resolution of ~100 m. Secondly, a direct comparison is hard to achieve because TC outer region rainband is highly asymmetric, therefore, even in pseudo-global warming experiments (Schär et al. 1996; Trapp et al. 2021), it is difficult to ensure the same timing for a preexisting convective system or moisture plume to impinge on a mountain. As a result, it is hard to tell whether orographic precipitation differences in the experiments are due to warming or timing (i.e., preexisting convective system may impinge onto the mountain at different stages of the life cycle of the system).

To overcome those difficulties, we adopted the LES method developed by Bryan et al., (2017) (hereafter B17) to simulate the TC environment. Instead of simulating the entire TC, this LES method only simulates a small ‘patch’ of a typhoon. The large-scale conditions that dominate the small ‘patch’ are specified using prescribed input parameters. Therefore, the large-scale conditions can be controlled to ensure direct comparisons. The warming experiments of the LES simulations are conducted with the pseudo-global warming method. (Rasmussen et al. 2011). We will focus on the intensity and distribution changes in orographic precipitation due to warming and investigate the underlying mechanisms.

2. Experiment setup

a. Typhoon Case

The LES simulations have an idealized environment based on a real typhoon event. Typhoon Vicente (2012) is one of the strongest typhoons affecting Hong Kong (HK) in recent decades and it caused more than 200 mm of precipitation over the two-day period during its passage over HK (Hong Kong Observatory 2012). According to observation data, the strongest precipitation in HK occurred 12 hours after Vicente’s landfall, when Vicente was more than 300 km away from HK. During the period from 05:00 UTC and 07:00 UTC on 24th July 2012, intense precipitation happened in Hong Kong.

During the two-hour intense precipitation period, Hong Kong happened to be located nearly due east of the cyclone center and indicated by the black square box in Supplementary Fig. S1. Therefore, for simplicity, no rotation of the wind profile was applied when setting the LES domain, and the tangential wind for the LES domain is assumed from due south. The square box in Supplementary Fig. S1 is centered at the Lantau Island of Hong Kong with a side length of 100 km. The Radius from the low-pressure center of the typhoon to the square center is 338.84 km. The Weather Research and Forecast (WRF) was used to simulate Typhoon Vicente in a previous study (Shi and Wang 2022) with horizontal resolution down to 1.6 km. We use the WRF simulation data to determine the input parameter profiles for base state and initial conditions of our LES simulation, by averaging relevant variables in the small square region in Supplementary Fig. S1 and over the 2-hour period with the most intense precipitation.

b. LES Simulation Setup

For our LES simulations, we use the TC environment parameterization method developed by Bryan et al. (2017) for the non-hydrostatic numerical model Cloud Model 1 (CM1, version 20.3) (Bryan and Fritsch 2002), which is an advanced tool for idealized LES and convection-permitting simulations. The LES domain consists of $N_x = 256$ grid points in the x direction with Δx = 200 m and a total length of L_x = 51.2 km. In the y direction, there are N_y = 512 grid points, with Δy = 200 m and a total length of L_y = 102.4 km. In the vertical direction, the model has N_z = 128 levels, with the grid spacing Δz stretching from 150 m near the surface to 500 m at the model top (L_z = 31.2 km). Periodic boundary conditions are applied at both horizontal directions. The Rayleigh damping is applied at heights above 22 km to avoid the excessive spurious reflection of gravity waves. The research is conducted mainly using the Thompson scheme (Thompson et al. 2008) as the microphysics scheme. For testing robustness of our conclusions, we also conducted some simulations with the Morrison microphysics scheme (Morrison et al. 2009) and documented the results in Section 6. For subgrid-scale turbulence parameterization, we used the TKE scheme (Deardorff 1980), and radiation is computed using the rapid radiative transfer model for general circulation models (RRTMG) (Iacono et al. 2008).

The B17 method was originally designed for simulating the wind profiles in the boundary layer of the outer region in TC. In this study, to investigate the interaction between convections and the mountain, the method is adapted, and the LES domain extends to 31.2 km in height. The TC boundary wind profile simulation model in B17 is based on the assumption that the small LES domain (embedded within the TC environment) is subject to centrifugal and advection accelerations that apply at scales large than the domain. The fundamental idea of B17 is to account for these large-scale conditions by specifying the vertical profile of gradient wind speed V, the radial gradient of gradient wind speed $\frac{\partial V}{\partial R}$, and a distance away from the tropical cyclone center R. Other than these parameters, to initiate the simulation, the vertical profile of potential temperature (θ), water vapor mixing ratio (q_v) are needed and shown in Fig. 1. B17 suggests that the $\frac{\partial V}{\partial R}$ can be related to $\frac{V}{R}$ through a decay rate n, $\frac{\partial V}{\partial R} = -n\frac{V}{R}$. The decay rate n for all types of tropical cyclones ranges from 0.04 to 0.64 (Mallen et al. 2005). We've found the precipitation intensity and distribution are insensitive to the selection of decay rate in this range. In view of this, a decay rate of 0.6 is used. The distance between the center of our research domain and the low-pressure center R is 338.84 km.

The large-scale pressure gradient in B17, originally designed for the atmospheric boundary layer, is derived from the gradient wind balance relationship. However, the gradient wind balance no longer holds at higher levels where there is no well-defined circular low-pressure center. Figure 1a shows the profile of meridional velocity V_{WRF} derived from the temporal and spatial mean of V from WRF output data, geostrophic wind V_{GEO} calculated based on the geostrophic balance, and V_{GRAD} calculated from the gradient wind balance. Below z_1 =11 km, V_{WRF} is consistent with V_{GRAD} except at the levels near surface, suggesting that in the lower and middle troposphere, the large-scale wind field is well approximated by the gradient wind balance in which the pressure gradient force is balanced by centrifugal force and Coriolis force. The inconsistency between V_{WRF} and V_{GRAD} at the lowest levels is due to the unaccounted surface friction and boundary-layer flux. Above z_2 = 15.5 km indicated by the green dotted horizontal line, the V_{WRF} oscillates around zero and shows good agreement with V_{GEO}, suggesting the wind field follows the geostrophic balance in which the large-scale pressure gradient is balanced only by the Coriolis force. At heights between z_1 and z_2, the wind field transitions from the gradient wind balance to the geostrophic wind balance, in which the centrifugal force gradually disappears.

In our setup of the large-scale pressure gradient in LES, for simplicity, we apply a linear decay coefficient α on the centrifugal force term and assume α decreases from unity at height z_1 to zero at height z_2 to represent the disappearance of centrifugal force. At levels above z_2, with no presence of centrifugal forces, we specify the large-scale pressure gradient force based on the geostrophic wind balance by setting α as 0. In the LES method of B17, mesoscale tendency terms are associated with the mesoscale flows in the tropical cyclone. Similarly, we apply the same decay coefficient α on the mesoscale tendency terms.

The original B17 method focuses on simulations of the wind profiles in the dry atmosphere. Moisture effects are neglected. Similar to Chen et al. (2021), nudging terms are applied to the tendency of temperature, specific humidity, and large-scale wind for the purpose of accounting for the effects of the large-scale circulation of typhoon environment. Details are be found in equations (1b) and (1c) from Chen et al. (2021). This nudging approach ensures that the large wind profiles, temperature, and moisture remain anchored throughout the simulations. The nudging relaxation timescale we used is 2 hours.

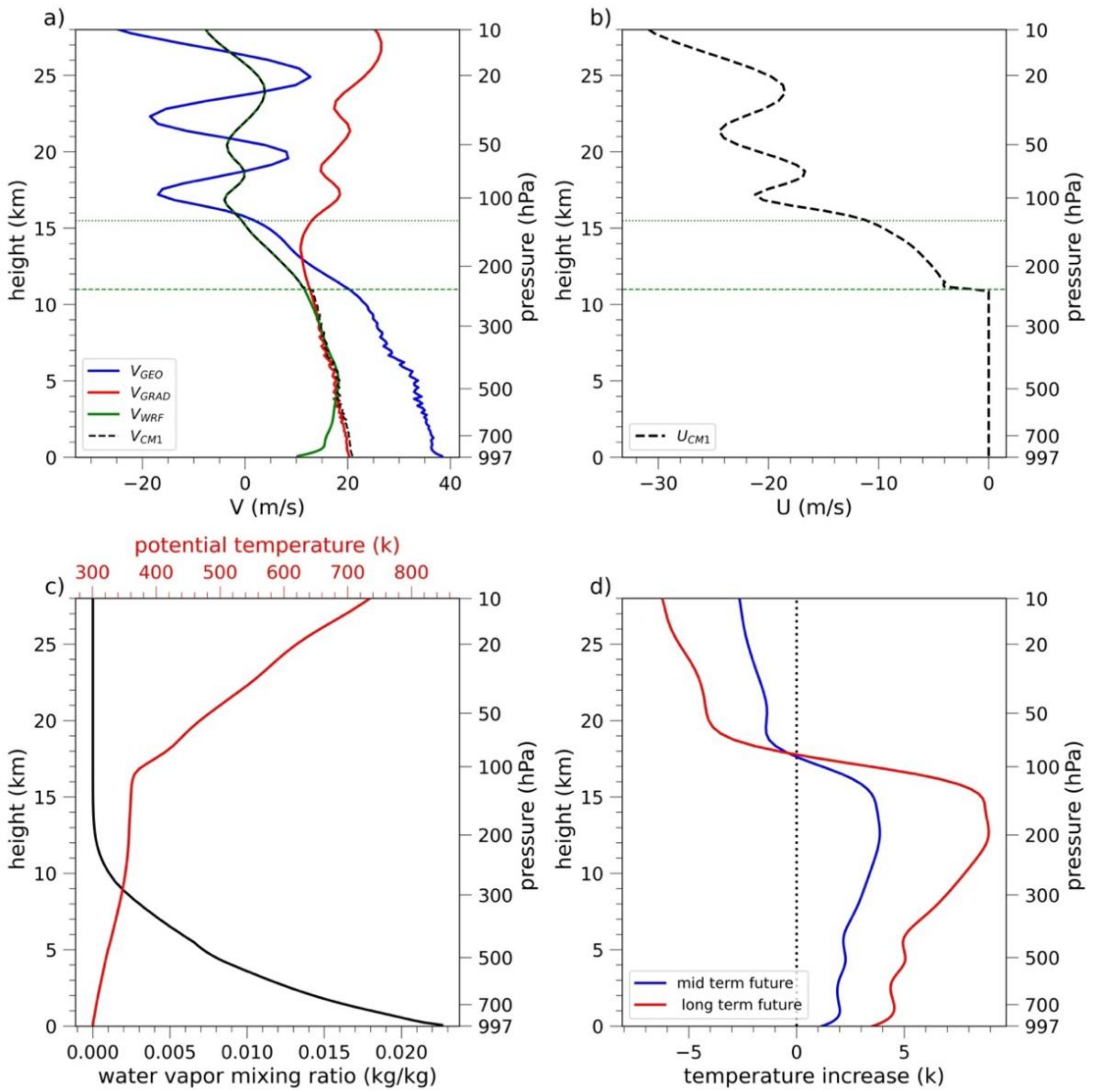

Fig. 1. (a) and (b) show the vertical profiles of horizontal wind (V and U). The mean V profile derived directly from the WRF simulation are denoted by the solid green lines. The mean V profiles calculated based on the geostrophic wind balance are shown as the solid blue lines and labeled as V_{GEO}. The V profile calculated based on the gradient wind balance is shown as the solid red line and labeled as and V_{GRAD}. The dashed black lines show the input V, U profiles used in our simulation and are labeled as V_{CM1} and U_{CM1}, respectively. (c) Potential temperature derived directly from the WRF simulation and water vapor mixing ratio (q_v). The q_v is derived assuming the atmosphere is saturated below 17 km. (d) The CMIP6 predicted mean temperature change between the present climate and the mid-term future climate (blue line) and mean temperature change between the present climate and the long-term future.

The terrain profile and initial flow field are specified by several parameters. The idealized bell-shaped terrain is set up to loosely mimic the Hong Kong topography which is featured by west-east-oriented mountains. The surface elevation Z_s of this bell-shaped mountain is specified as

$$Z_s(y) = \begin{cases} \frac{h_0}{2}\left(1 + cos\left(\pi\left(\frac{y - y_m}{a}\right)\right)\right) & \text{if } y_m - a < y < y_m + a \\ 0 & \text{else} \end{cases} \quad (1)$$

where the maximum height h_0 is 1 km, half-width a is 10 km, $y_m = 0$ is at the center of the domain in the meridional direction. The surface area where $Z_s = 0$ is set as ocean surface. The mountain is symmetric in the zonal x direction.

c. Warming Experiments

In the warming experiments, we've conducted pseudo-global warming by adding the temperature change predicted by the SSP5-8.5 (Shared Socioeconomic Pathway) warming scenario from the Coupled Model Intercomparison Project phase 6 simulations (CMIP6) onto the control simulation temperature profile. The current climate state is defined as the average for the period of 2015-2020, the mid-term future as the period of 2050-2060, and the long-term future as the period of 2090-2100. The temperature is averaged over the larger domain centered at Hong Kong, ranging from 110 to 120 degree in longitude and 15 to 25 degree in latitude. The surface warming relative to the present climate is 1.18 and 3.53 K, respectively, for the climate of the mid-term future and long-term future. Figure 1d shows temperature change between present climate and future climates. The temperature anomaly profiles are characterized by the strongest warming happening in the upper troposphere, and the cooling happening in the stratosphere, consistent with previous studies (e.g., Ji et al., 2020). In the troposphere, the upper levels exhibit stronger warming than the low levels, suggesting a more stable atmosphere under warming. In terms of the input of vertical profile of q_v, we assume the relative humidity profile remains constant over the warming. Therefore, we have 3 groups of simulations: present, mid-term future, and long-term future climate. Each simulation was integrated for 36 hours with an output interval of 10 min. The first 12 hours are discarded as the spin-up period. In the analysis below, unless specified, otherwise the temporal average is taken over the period from hour 12 to hour 36.

3. Orographic Precipitation and Traveling Convective System

a. Precipitation Distributions

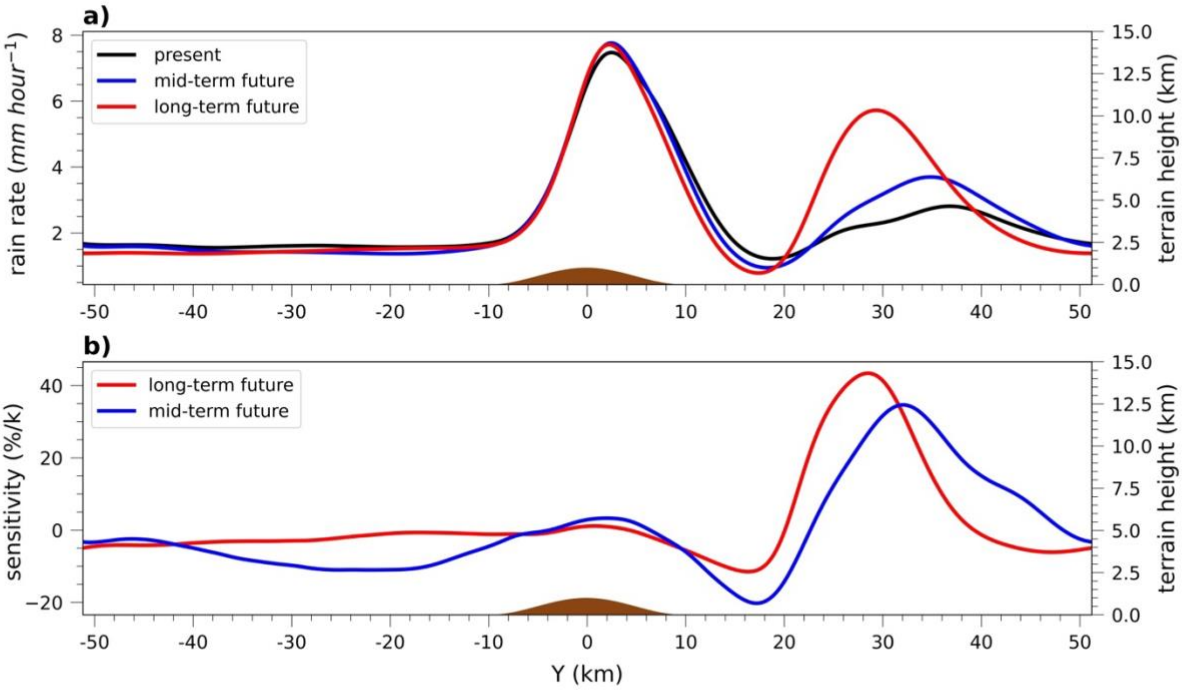

Fig. 2. (a) The zonal and temporal mean precipitation distribution in the simulations of present, mid-term future, and long-term future climate. (b) the corresponding precipitation sensitivity to warming in (a). The sensitivities in (b) are defined relative to the present climate.

The zonal (x-direction) and temporal mean precipitation distributions are shown in Fig. 2. In the simulation of the present climate, two local precipitation maxima can be identified. The first precipitation maximum is located on the lee slope of the mountain and the second precipitation peak is in the downstream of the mountain at around 37 km. The simulations for mid-term future and long-term future climate exhibit qualitatively similar precipitation maxima patterns with peaks on the lee slope and in the downstream region.

The first precipitation peak on the mountain slope barely changes (shown in Fig. 2a) with warming. By contrast, the second downstream region precipitation peak shifts upwind towards the mountain and intensifies substantially with warming. Figure 2b shows the corresponding precipitation sensitivity, which is defined as the change relative to the present climate, normalized by surface temperature increase. The sensitivity near the first peak is close to zero. However, the precipitation sensitivity related to the second precipitation maximum has shown large sensitivity and can reach up to 34.65% K^{-1} in the mid-term future and up to 43.41% K^{-1} in the long-term future. The response to warming is discussed in depth in the next section. The remaining discussion of this section identify and explain essential mechanisms involved in shaping the distribution pattern of precipitation in our simulations.

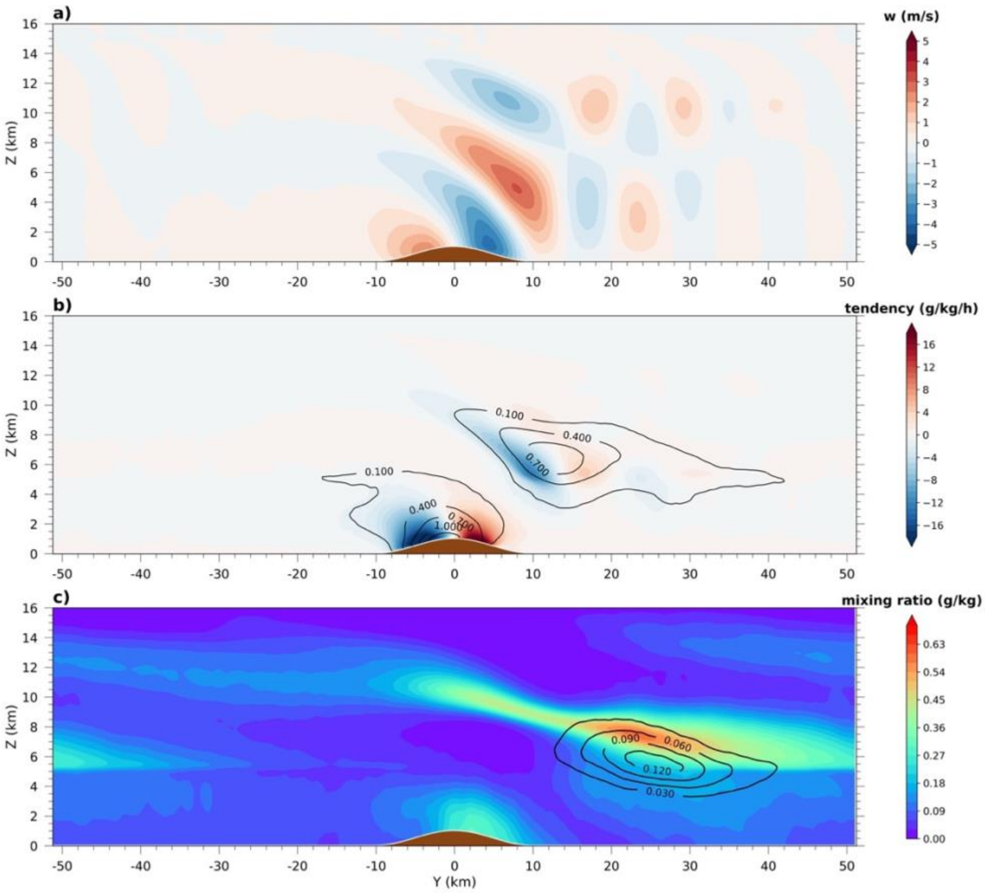

Fig. 3. The zonal and temporal mean of (a) vertical velocity (w), (b) water vapor mixing ratio tendency due to microphysics (color shading), the sum of cloud ice (q_i) and cloud water (q_c) mixing ratio (contours, unit in g/kg), (c) mixing ratio of precipitation hydrometeors which include rain, graupel and snow (color shading) and graupel mixing ratio alone (contours, unit in g/kg).

Here, the mean states are firstly investigated. Figure 3a shows the zonal and temporal mean of vertical velocity. Two areas exhibit strong updrafts: 1) over the upwind slope of the mountain and 2) over the lee slope of the mountain centered at y = 8 km, z = 5 km. In downstream region away from the mountain, the averaged vertical velocity oscillates between positive and negative velocities, suggesting the presence of mountain-induced gravity waves. Those stationary updrafts and downdrafts weaken with distance away from the mountain and are confined below the tropopause, which indicates these lee waves are trapped, or at least partially trapped. The zonal and temporal mean of water vapor tendency due to microphysics ($\dot{q}$) is shown in Fig. 3b. The negative $\dot{q}$ value indicates condensation and deposition whereas the positive $\dot{q}$ values indicate evaporation and sublimation. The areas that exhibit strong updrafts also show strong condensation-and-deposition rates. The two strong condensation-and-deposition centers caused by the strong stationary updrafts correspond to the two cloud centers indicated by the sum of cloud water mixing ratio (q_c) and ice mixing ratio (q_i). It is noteworthy that the two cloud centers exist throughout our simulation and are closely related to two precipitation maxima.

As shown in Fig. 3c, the two precipitation peaks also correspond to the two regions with high mixing ratios of precipitation hydrometeors (q_p). The q_p is the sum of mixing ratio of rainwater (q_r), graupel (q_g) and snow (q_s). The high q_p region over the lee slope of the mountain extends from the surface to the lower troposphere, suggesting ice phase process is not involved much in the formation of the first precipitation peak. In contrast, the high q_p area located in the downstream of the mountain extends from the surface up to upper troposphere. A significant amount of graupel is found above the downstream precipitation region, indicating the involvement of the ice and mixed phase processes in the formation of the second precipitation peak. In the following subsection, we will show that the formation of the two precipitation maxima is related to the interaction between the traveling mesoscale disturbances and mountain wave-forced ascents, though the roles of them are different for the two precipitation maxima.

c. Traveling Mesoscale Disturbances

The Hovmöller diagram of the zonally averaged surface precipitation shows a precipitation pattern suggesting northward traveling mesoscale disturbances (Fig. 4). The mesoscale disturbances travel northward with a period of about 2 hours. In each cycle, the zonal mean precipitation features the two precipitation maxima and a rain shadow region sandwiched by the two-precipitation maxima. Notably, little-precipitation windows can be identified for every location. The little-precipitation windows suggest that precipitation maxima are not purely the result of the mean flow advection of hydrometeors produced in the two cloud formation centers in Fig. 3b. Without the superposition of the traveling mesoscale disturbances on the mean flow, little surface precipitation is generated, probably because of insufficient microphysical conversion time (Zängl 2008) or evaporation when the precipitation hydrometeors fall out of cloud at a high level (Kirshbaum and Smith 2008).

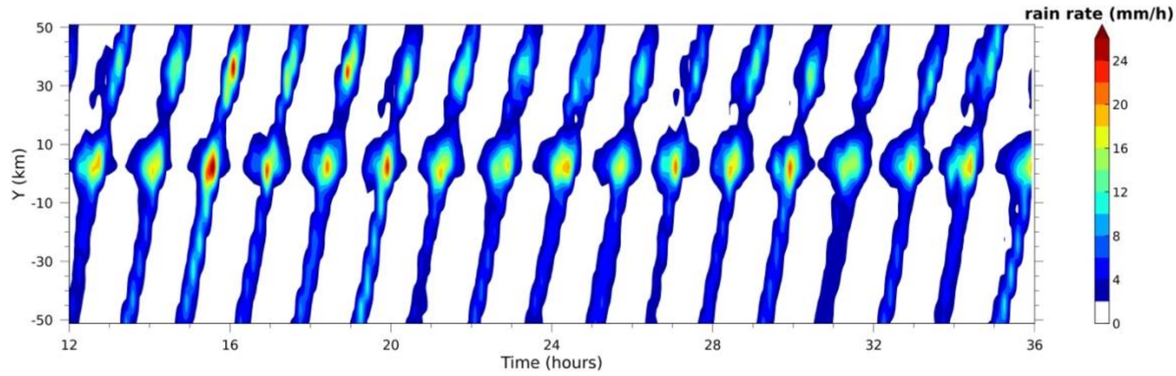

Fig. 4. The Hovmöller diagram of the zonally averaged surface precipitation in the present climate simulation.

To further illustrate the relations between the two condensation centers and the two precipitation maxima, regression analysis relating surface precipitation to hydrometeors (q_p, q_g, q_i+q_c) and $\dot{q}$ has been conducted. Following Adames and Wallace (2014) ,the regression map for each variable is derived from the equation, $\mathbf{D} = \mathbf{S}\ \mathbf{P}^{\mathbf{T}}$, where $\mathbf{D}$ is the regression pattern with dimensional units, for a two-dimensional matrix $\mathbf{S}$ that represents a variable field, and $\mathbf{P}$ is a standardized time series of the variable being regressed upon.

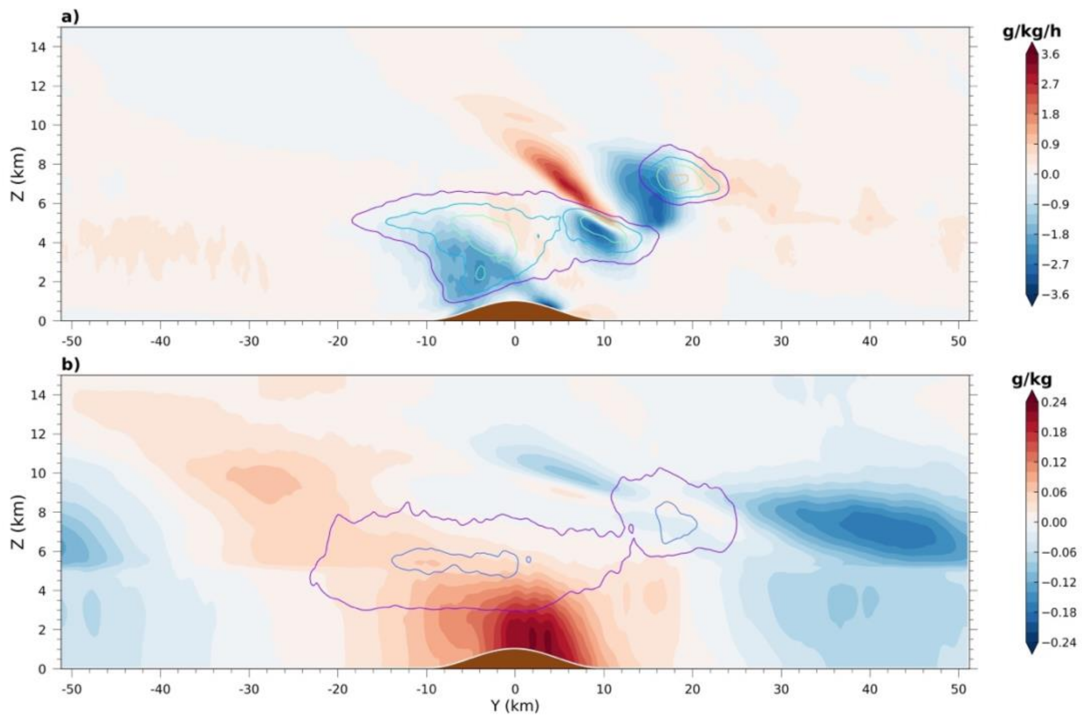

Fig. 5. Regression onto the standardized time-series of mean precipitation over the mountain between $y = -14$ and $y = 10$ km in the present climate simulation for (a) $\dot{q}$ (color shading) and $q_i + q_c$ (contours) and (b) q_p (color shading) and q_g (contours). Contour interval in (a) is 0.04 g/kg and the purple contours indicate 0.04 g/kg. Contour interval in (b) is 0.01g/kg and the purple contour indicates 0.001 g/kg.

The precipitation maximum over the mountain is related to the interaction between the cloud above the windward slope of the mountain and the traveling mesoscale disturbances. The regressed $\dot{q}$ and $q_c + q_i$ in Fig. 5a show that low-level cloud formation is enhanced when there is positive precipitation anomaly over the mountain. Noting that the regressed pattern represents anomalies to be added to the stationary pattern in Fig. 3 when there is positive precipitation anomaly on the mountain surface. Figure 5a suggests that when the mesoscale disturbance reaches the mountain it probably triggers or enhances orographic convection substantially and therefore enhance surface precipitation.

Meanwhile, the regression of precipitation hydrometeors (Fig. 5b) shows a second center of positive anomaly at about 9 km above the surface and 30 km upstream of the mountain. The upper level q_p anomaly extends downward until reaching the freezing level, but it also extends downwind and connects with the low-level cloud and precipitation. Therefore, the formation of effective precipitation over the mountain is likely also affected by the seeder-feeder mechanism (Bergeron 1960). The upper-level regression anomaly in Fig. 5b suggests stratiform precipitation in the upper and middle troposphere related to deep convective system falls from above and enhances accretion in the low-level orographic cloud above then windward slope. This regression pattern feature is also consistent with Fig. 4, which shows that the precipitation over the mountain becomes notable before the main travelling precipitation system reaches the mountain. The reason for which no deep convection signal exists upstream of the mountain (from $y = -30$ km to $y = -20$ km) in the regression pattern is probably because the regression has zero time lag, which makes the regressed pattern more representative for features when precipitation over the mountain is maximized.

Figure 6 shows the regressed fields related to the precipitation in the downstream region, which suggests the interaction between cloud induced by the mid-tropospheric orographic ascent above the lee slope of the mountain (Fig. 3a) and the traveling convective system. The negative anomaly of regressed $\dot{q}$ and positive anomaly of regressed $q_c + q_i$ in Fig. 6a suggests that deep convection exists when surface precipitation is enhanced in the downstream region. The regressed q_p in Fig. 6b shows two maxima in the downstream region, one in the lower troposphere and the other in the upper troposphere at about 8 km. The upper-level maximum is related to the local deep convection. Interestingly, the lower-level maximum is somewhat separated from the upper-level maximum, suggesting there is an additional mechanism that enhances the lower-level precipitation hydrometeors mixing ratio. The presence of mid-troposphere ascent and cloud formation above the lee slope of the mountain (Fig. 3b) can produce a significant amount of precipitation hydrometeors which drift downstream with the mean flow. As those hydrometeors fall into the lower and middle part of the convective system which develops in the downwind region, they enhance collision-and-coalescence or accretion like in the conventional seeder-feeder mechanism. We call this mechanism pseudo-seeder-feeder (PSF) mechanism because here convection and terrain forced ascents play roles differing from what they have in the conventional seed-feeder mechanism. The PSF mechanism is likely more important to local precipitation enhancement in the downwind region than over the mountain because the regression of graupel mixing ratio onto the second precipitation maximum in the downstream region (Fig. 6b) exhibits a substantially stronger signal than the same regression onto the first precipitation maximum over the mountain top (Fig. 5).

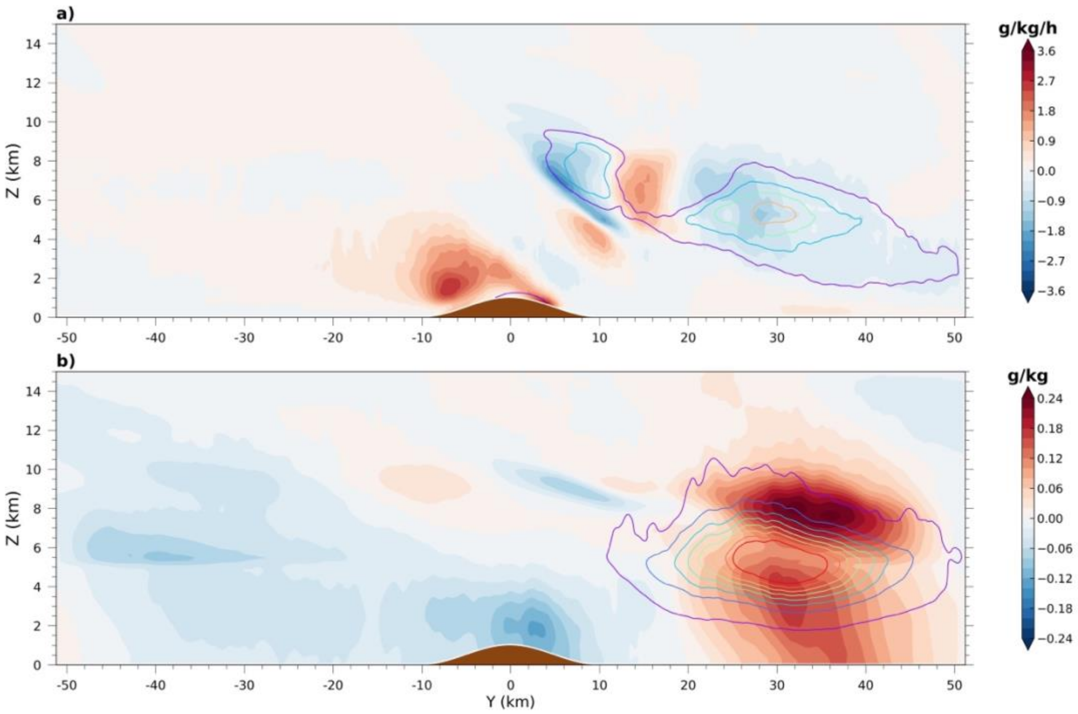

Fig. 6. Same with Fig. 5, except that the regression plots are based on the time-series of the mean precipitation in the downstream region between y = 21 and y = 45 km.

4. Precipitation Responses to Warming

As discussed in Section 3a, under warming, the precipitation over the downstream region and the mountain has strikingly different responses to warming. In this section, these two regions are investigated separately to understand their responses to warming. Below, we calculate how the condensation and deposition change in the cloud formation region and how precipitation efficiency responds to warming. The impact of mountain waves is also discussed.

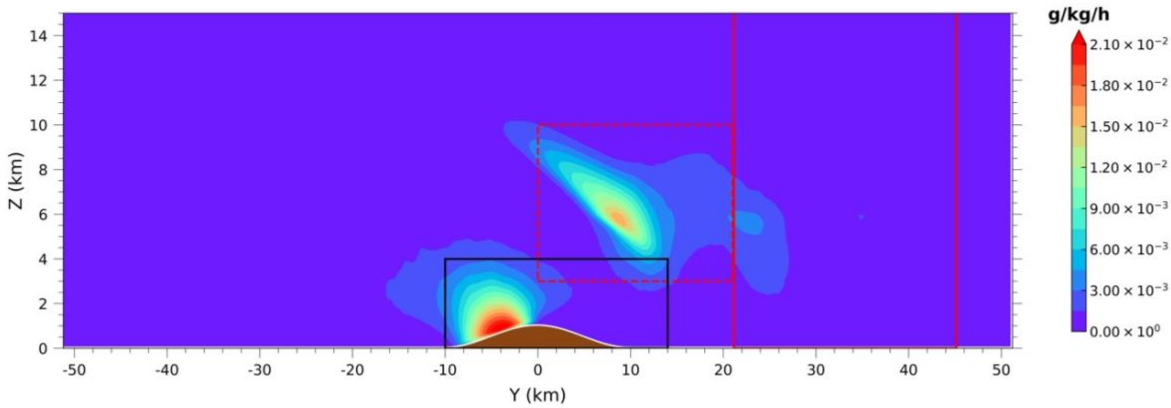

Fig. 7. The zonal and temporal mean of condensation rate in the simulation of present climate. The black box over the mountain is for the analysis of precipitation over the mountain, the region bounded by red lines between *y* = 21 km and *y* = 45 km is for the analysis of precipitation over the downstream region. The red box between *y* = 0 km and *y* = 21 km wraps the condensation center in the lee of mountain.

a. Over-Mountain Precipitation

For the over-mountain precipitation region, the downstream transport of hydrometeors in a strong wind environment cannot be ignored because we are considering relatively small regions. We use the black box shown in Fig. 7 for a budget analysis. The box is bounded between *y* = −10 km and *y* = 14 km to include the first precipitation maximum and capped vertically at 4 km to avoid the inclusion of the lee condensation and deposition center in mid-troposphere to which the first precipitation maximum is unrelated. The time averaged surface precipitation (P) at the bottom of this box satisfies

$$P = C_{net} + F_{in} - F_{out} + R \qquad (2)$$

where C_{net} is the volume integrated rate of net condensation and deposition, F_{in} (F_{out}) is the flux of condensates, including both non-precipitation and precipitation particles, into (leaving) the box through upstream (downstream) boundaries. C_{net}, F_{in}, and F_{out} are normalized with the bottom surface area of the box. R denotes the residual term due to ignoring surface evaporation and storage of hydrometeors in the air. This residual term can be minimized when we take the time average of a relatively long period so that the storage of hydrometeors in the air can be ignored. Surface evaporation is also ignored because of its little contribution. The residual term only accounts for around 5% of the surface precipitation (Supplementary Table S1), suggesting the approximate balance between P and $C_{net} + F_{net}$ inside the box. Including the influx of hydrometeors from upwind direction into the box, the PE is redefined as

$$\mathrm{PE} = \frac{P}{F_{in} + C} \tag{3}$$

where F_{in} is influx convergence into the box, C is the volume integrated rate of condensation and deposition inside the box. Both C and F_{in} are normalized with the bottom surface area of the box. For this over-mountain precipitation region, C is much larger than F_{in}. Denoting the surface temperature by T_s, the total precipitation sensitivity can be decomposed as

$$\begin{aligned} \frac{1}{P}\frac{\partial P}{\partial T_s} = \frac{\partial lnP}{\partial T_s} = \frac{\partial\, ln(\mathrm{PE} \cdot (C + F_{in}))}{\partial T_s} = \frac{\partial ln\,(C + F_{in})}{\partial T_s} + \frac{\partial ln\,(PE)}{\partial T_s} \\ = \frac{\partial (C + F_{in})}{(C + F_{in})\,\partial T_s} + \frac{\partial \mathrm{PE}}{PE\,\partial T_s} \end{aligned} \tag{4}$$

The precipitation sensitivity over the mountain is the sum of the sensitivity of $C + F_{in}$ and that of PE. Table 1 is the average sensitivity obtained by comparing the simulations of present and mid-term future and that by comparing those of present and long-term future. As shown in Table 1, both terms have shown sensitivities less than 1% K^{-1}. Therefore, the weak precipitation response to warming is due to small sensitivities of PE, F_{in}, and C. The C in the black box has shown a slight decrease with warming. This negative sensitivity is at odds with the expected positive sensitivity in previous studies (e.g., Siler and Roe, 2014). To understand the negative condensation sensitivity to the warming, the change of C in the black box is further decomposed to thermodynamic and dynamic contributions based on the methodology in Shi and Durran (2015). The thermodynamic contribution is related to the change in the moist adiabatic lapse rate of saturation water vapor specific humidity (γ) due to temperature increase, and the dynamic contribution is related to the change in the vertical velocity (Muller and Takayabu, 2020; Shi and Durran, 2015). Our calculation found that the thermodynamic contribution is at around 2.11% K^{-1}, which is offset by the dynamic contribution at around −2.68% K^{-1}. The temperature of the upslope condensation center in our black box ranges from ~270 to ~300 K. Our calculation of thermal contribution to the warming is consistent with the γ sensitivity in that temperature range (shown in Fig. 12 of Shi and Durran (2014)).

Table 1: Sensitivity with respect to surface warming over the mountain region (indicated by the black solid box in Fig. 7): precipitation (P), condensation (C), influx to the right boundary of black solid box (F_{in}), precipitation efficiency (PE). C_t is the thermodynamic contribution of C. C_d is the dynamic contribution of C.

Sensitivity (% K^{-1})	P	C	F_{in}	C+F_{in}	PE	C_t	C_d
Mid-term	0.69	-0.29	0.66	-0.14	0.84	2.16	-2.55
Long-term	-1.81	-1.32	1.00	-0.97	-0.86	2.07	-2.81
Mean	-0.56	-0.80	0.83	-0.56	-0.01	2.11	-2.68

The negative dynamic contribution is related to the weakening of vertical velocities over the windward slope of the mountain under warming. The zonal and temporal mean of vertical velocities are shown in Fig. 8. The mean vertical velocity maximum over the windward slope of the mountain does not exhibit appreciable change but the depth of the ascending layer shallows in response to warming. The weakening of vertical velocities is probably related to the response of mountain wave to the increased stability (Shi and Durran 2015), which is caused by the amplified warming in the upper troposphere. Additionally, negative dynamic contribution is also found in the previous study of extreme convective precipitation in the tropics (Muller et al., 2011).

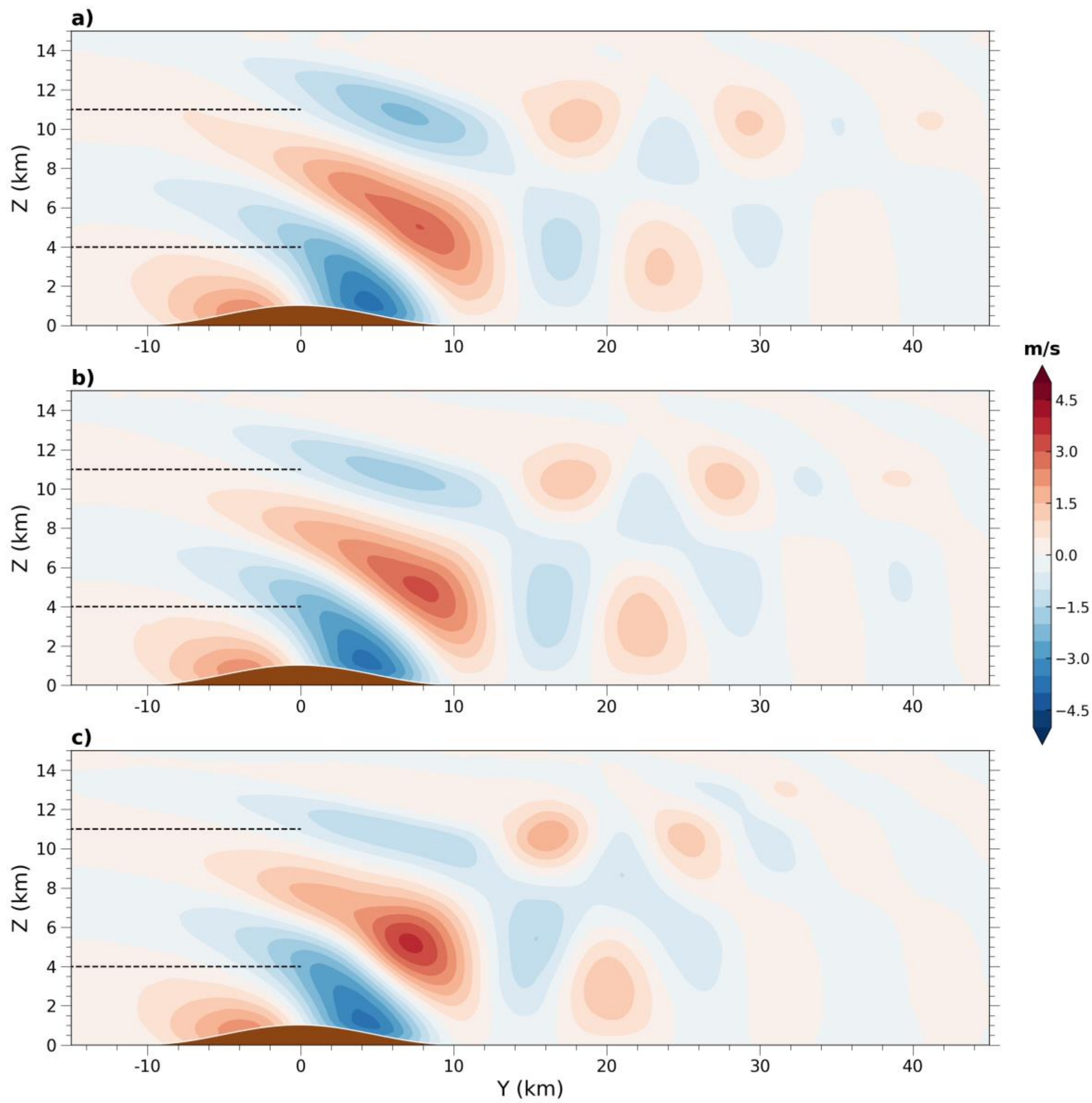

Fig. 8. The zonal and temporal mean of vertical velocities of simulations of the climate of the present (a), mid-term (b), and long-term future (c). The black dash lines at 4 km and 11 km are for height references.

b. Downstream Region Precipitation.

In the downstream precipitation *maximum region*, we conduct the same *budget* analysis *for* precipitation efficiency and hydrometeor production. The budget box is defined starting from 21 km to 45 km in the *y* direction, which is indicated by the red solid vertical lines in Fig. 7. The downstream precipitation statistics are partly shown in Supplementary Table S2.

The precipitation in the downstream has exhibited substantial change due to warming, and as shown in Table 2, the mean precipitation sensitivity is at 18.16% K^{-1}. The local C has exhibited little change and its mean sensitivity to the warming is at -0.29% K^{-1}. In contrast, the F_{in} sensitivity is at 9.25% K^{-1}, suggesting the increased influx with warming. The F_{in} increase can be explained by the increased condensation and deposition rate in the lee-slope mid-troposphere condensation-and-deposition center C_2 (denoted by the red dashed box in Fig. 7). The sensitivities of C_2 are consistent with the F_{in} (Table 2), indicating that the influx increase is due to the amplification of C_2. We further decompose the change of the C_2 into thermodynamic and dynamic contributions. The dynamic contribution is slightly positive and at 1.04 K/%, while the thermodynamic contribution is at 7.20 % K^{-1}, revealing that the increase of influx is primarily from thermodynamic contribution. The thermodynamic sensitivity of C_2 is larger than that of the low-level, windward slope condensation center because 1) the sensitivity of γ to temperature is higher at colder temperatures (Fig. 12 of Shi and Durran (2014)) and 2) mid-troposphere exhibits stronger temperature increase than the surface.

Table 2: Sensitivity with respect to surface warming in the downstream region (indicated by the red solid box in Fig. 7): precipitation (P), condensation (C), influx to the right boundary of red solid box (F_{in}), precipitation efficiency (PE). The C_2 is condensation rate of the red dashed box region shown in Fig. 7. C_{2t} is the thermodynamic contribution of C_2. C_{2d} is the dynamic contribution of C_2.

Sensitivity (% K^{-1})	P	C	F_{in}	$C+F_{in}$	PE	C_2	C_{2t}	C_{2d}
Mid-term	19.37	-0.83	12.02	6.32	12.14	11.52	7.99	1.29
Long-term	16.96	-1.42	6.49	2.46	13.34	6.80	6.41	0.79
Mean	18.16	-0.29	9.25	4.39	12.74	9.16	7.20	1.04

Following Eq. (4), the precipitation sensitivity in the downstream region can also be decomposed into the sensitivity related to PE change and source of hydrometeors ($C + F_{in}$). The change in precipitation efficiency is dominant at 12.74% K^{-1}, while the change of the sum of local condensation and influx plays a secondary role at 4.39% K^{-1}(Table 4). The high PE sensitivity suggests enhancement of the pseudo seeder-feeder effects. This enhancement is probably due to the increases of F_{in} into the downstream region that can be further attributed to the amplified lee cloud formation center C_2.

The high precipitation peak sensitivity in the downstream region is also partially due to the upwind shift of the second precipitation maximum, which exhibits ~10 km between the present and long-term future simulations. This upwind shift of downstream region precipitation peak is related to the upwind shift of mean state mountain waves and the lifting of freezing level in the warmed climates. The mean state wave patterns of vertical velocities are shown in Fig. 8. The updraft centered at $y \approx 24$ km in the simulation of present climate moves upwind to 20 km in the simulation in of long-term future climate. With the upwind shift of mean state waves, the region which is prone to the development of new convection in the downstream region moves upwind. The hydrometeors drifting from the lee mid-troposphere center will travel at a shorter distance and experience less evaporation or sublimation before seeding the low-level convection in the downstream region. In addition, as the freezing level shifts upward, the fraction of liquid-phase hydrometeors increases in the lee slope mid-troposphere cloud center. As a result, the seeder hydrometeors fall at relatively larger terminal velocity and tend to interact with the low-level feeder clouds earlier at a shorter travel distance in the horizontal direction.

5. Upwind Shift of Trapped Lee Waves

The upwind shift of downstream precipitation maximum is, at least partially, related to the upwind shift of trapped lee waves, which is investigated in this section with the numerical methods of Durran et al. (2015), which search for linear modes that represent trapped waves in the lee of a mountain.

We used a 3-layer setup for the linear model, with layer interfaces at 9 km and 16 km for the present climate, and 10 km and 17 km for the long-term future climate. The squared Brunt–Väisälä frequency N^2 for the present climate setup is 1.2, 0.5, and 5 × 10^{-4} s^{-2} for the three layers from bottom to top. For the long-term future scenario, the mid-layer N^2 increases from 0.5 × 10^{-4} s^{-2} to 0.8 × 10^{-4} s^{-2}. The N^2 in other layers is the same as the present climate setup. The horizontal wind is assumed as 20 m/s at all layers. This assumption of the wind profile is the main caveat that we cannot avoid because in three-dimensional CM1 simulations we have both u and v velocity components, but we can only have one horizontal direction in the two-dimensional model. These parameters are idealization based on the simulation data. The method of Durran et al. (2015) yields two trapped modes for each setup. However, one of them has only one vertical velocity extremum in the troposphere and is not consistent with the mean velocity pattern in Fig. 8.

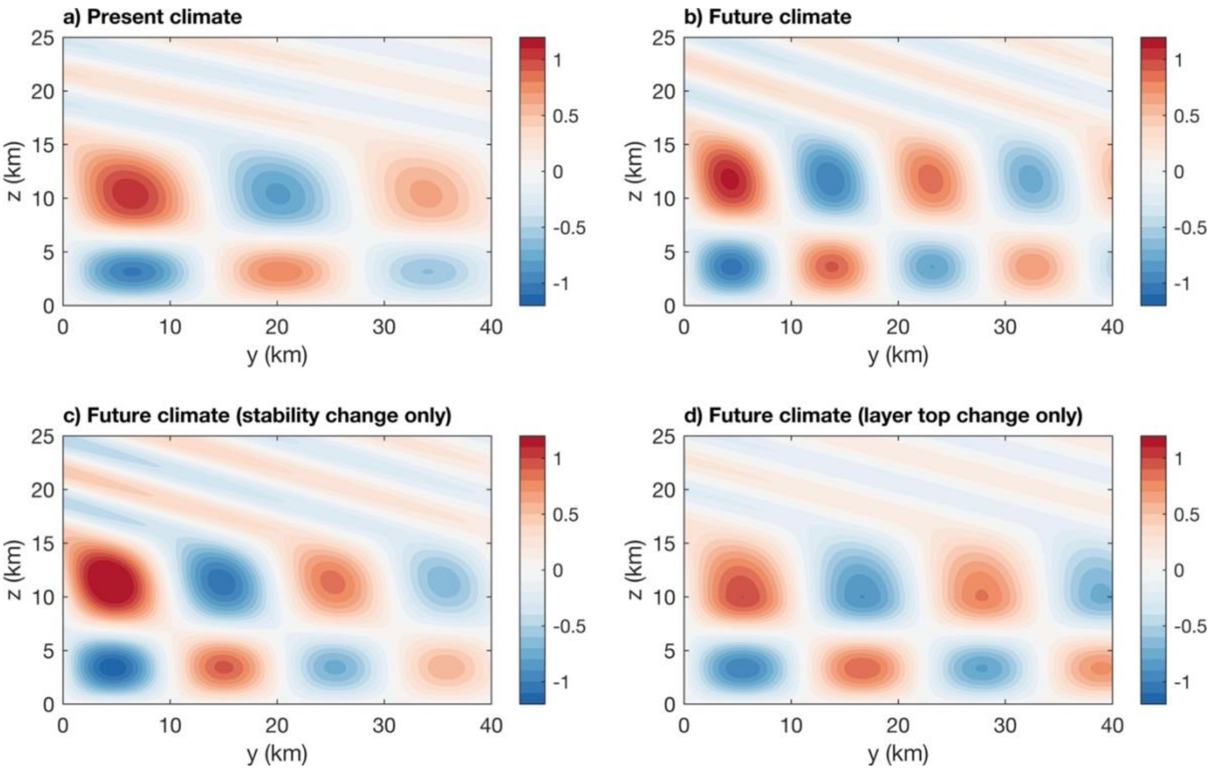

Fig.9. Contours of w in a vertical cross section obtained using numerical method developed by Durran et al., (2015) and the vertical velocity is normalized. a) calculation based on the mixed moist instability and the layer interfaces of the present climate. b) calculation based on the mixed moist instability and the layer interfaces of the long-term future climate. c) calculation based on the mixed moist instability of the long-term future climate but the layer interfaces of present climate. d) calculation based on the mixed moist instability of the present climate but the layer interfaces of the long-term future climate.

Figure 9 shows the relevant solution of the trapped mode, which indeed exhibits upwind shift under global warming. The upwind shift of trapped lee waves is due to the decrease in the horizontal wavelength of trapped lee waves. The resonant wavelength decreases from the 27.6 km in the present climate setup to the 18.7 km in the long-term future climate set-up. The effects of increasing upper troposphere static stability and tropopause height are separately evaluated in Fig. 9c and 9d, while Fig. 9b is the composite effect. Both factors contribute to the decrease of the resonant wavelength. If we only change the stability N^2 while keeping the layer interface heights unchanged, the resonant wavelength decreases to 20.4 km. If the layer interfaces are changed while the stability is kept constant, the resonant wavelength decreases to 22.1 km. Therefore, the stability enhancement probably seems more important to induce the upwind shift of trapped lee waves, though the role of tropopause lifting is also nonnegligible.

6. Robustness of Results

The robustness of our results is tested using the Morrison microphysics scheme and a narrower mountain (NM). Consistently, the highest precipitation sensitivity happens in the downstream region (Fig. 10).

Figure 10a shows the zonal and temporal rainfall distribution in the simulations using the Morrison microphysical scheme. Different from the Thompson scheme, the second precipitation maximum in the downstream of the mountain in Morrison is weak and virtually non-existent. The discrepancy in the occurrence of precipitation maximum in the downstream region in the simulation of present climate is probably related to the different liquid to solid ratios of the seeder particles in these two microphysical schemes. The transition of seeding precipitation particles from the solid phase to the liquid phase happens in an earlier stage in the Morrison scheme (Supplementary Fig. S2). As a result, a higher liquid ratio in the seeding precipitation particles is expected in the Morrison scheme. Given the ice particles involved processes are more efficient in producing rainwater (Kirshbaum and Smith 2008), the PSF in the Morrison scheme is expected to be weaker and thus may fail to create the downstream precipitation peak.

Experiments using a narrower mountain with a half-width of 5 km (NM) are also tested with different microphysical schemes. Previous experiments using the 10 km mountain half-width are referred as the wide mountain (WM). The two cloud formation centers induced by the NM are much smaller (Supplementary Fig. S2). With smaller cloud formation centers, both the traditional seeder-feeder effects and PSF are weakened and therefore weaker precipitation is resulted in the NM simulations (shown in Fig. 10a and Fig. 10c). Interestingly, in the present climate of NM, both microphysics schemes do not produce the downstream precipitation maximum. This is probably because the weaker lee cloud formation center supplies fewer drifting hydrometeors which serve as seeder particles in PSF. Although the solid particle fraction in present climate is higher than that in warmed climates. This advantageous condition for enhanced PSF is outweighed by the weaker lee cloud formation center in the present climate.

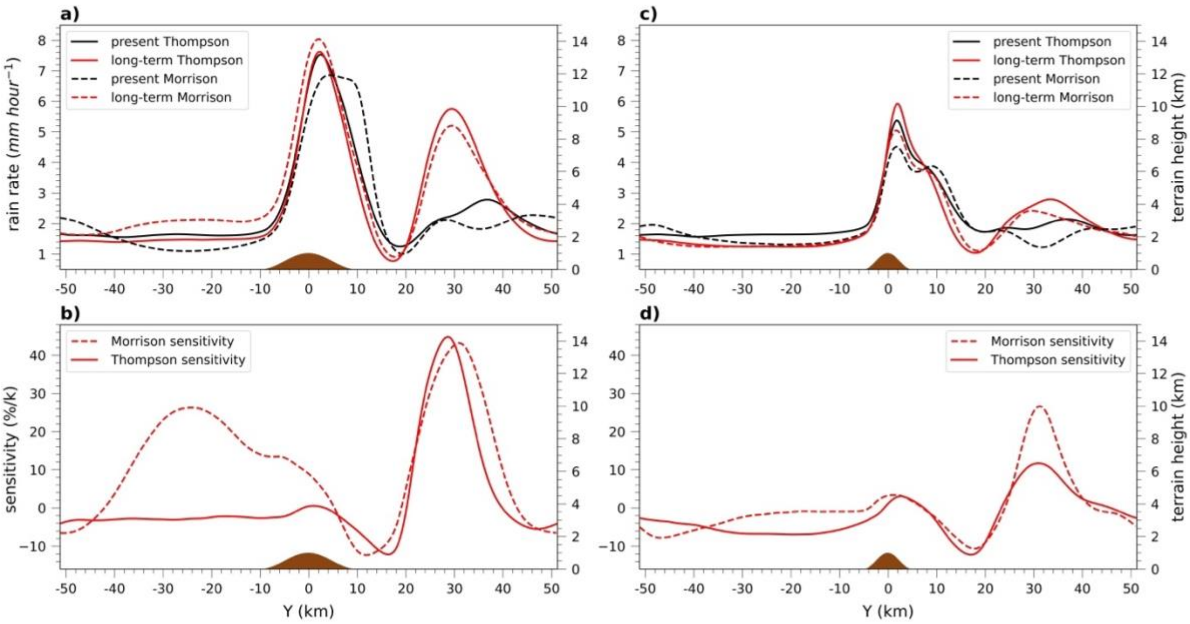

Fig. 10. The temporal and zonal mean precipitation in the simulation of present and long-term future climate, and corresponding precipitation sensitivity using different half widths of the mountain range and microphysical schemes. The half width of 10 km using the Thompson and Morrison scheme (a), (b). The half width of 5 km using Thompson scheme and Morrison scheme in (c) (d).

7. Conclusions

The global warming response of orographic precipitation induced by the interaction between a typhoon's outer circulation environment and a mountain is estimated with pseudo-global warming experiments using LES. In our control simulation for the present climate, the cross-mountain direction precipitation distribution exhibits two maxima with first maximum located on the lee slope of the mountain and the second weaker maximum in the region downstream of the mountain. The first precipitation maximum is related to the conventional seeder-feeder effect and enhanced convection by the mountain. The second maximum is related to a pseudo seeder-feeder effect in which the seeder cloud is the mountain wave induced mid-troposphere cloud above the lee slope and feeder cloud is the middle and lower part of traveling precipitation system in the downstream region.

In response to the warming, the first rainfall maximum exhibits almost no change because both condensation rate and precipitation efficiency have negligible changes. This weak sensitivity of condensation rate is because the positive thermodynamic contribution is canceled by the negative dynamic contribution. In contrast, the second rainfall maximum shifts upwind and intensifies significantly. The precipitation sensitivity in the downstream region (21 km to 45 km away from mountain) is at 18.16% K^{-1} on average and has a maximum sensitivity up to 43.41% K^{-1}. In the downstream region, the accelerated rainfall intensification is attributed to the substantial amplification of the condensation-and-deposition center in the mid-troposphere above the lee slope, where the temperature is lower than the low-level condensation center and the thermodynamic sensitivity is relatively high. This enhancement increases the downstream precipitation by increasing the influx of hydrometeors and thereby enhancing the pseudo seeder-feeder effect.

The high peak sensitivity in downstream region precipitation is also partially due to the upwind shift of the precipitation maximum, which is caused by the upwind shift of the trapped lee waves and the lifting of the freezing level. The upwind shift of trapped lee waves is further corroborated by a three-layer linear mountain wave model, which shows a decrease in the resonant wavelength of the trapped lee wave due to the lifting of the layer interfaces and the increase in upper tropospheric stability.

The robustness of our results is tested with a narrower mountain and a different microphysics scheme. Consistently, all simulations in warmed climate show relatively larger precipitation sensitivity in the downstream region. Lee side regeneration of convection has been investigated in previous studies (Houze 2012). However, the contribution from mountain wave induced lee-slope mid-troposphere cloud to the downstream region precipitation is neglected in previous studies, probably because precipitation particles may evaporate completely before reaching low-level cloud and thereby the pseudo seeder-feeder mechanism is not activated.

Our estimation of future orographic precipitation in the typhoon outer region environment shows that the greatest precipitation sensitivity happens in the downstream area, while the precipitation maximum over the mountain stays almost unchanged with warming. Although these are idealized experiments, our findings suggest plausible mechanisms by which the precipitation maximum in the downstream region of mountain barriers may emerge and intensify substantially under warming. Those mechanisms warrant further investigations focusing on the downstream region of mountains in the context of flooding risk management under climate change.

Acknowledgments.

This research was funded by the Research Grants Council of Hong Kong SAR, China (Project Nos. AoE/E-603/18 and HKUST 26305720).

Data Availability Statement.

The CM1 code and namelist files can be found at https://github.com/JiananChenUST/Chen-and-Shi-2023-.git. The initial input profiles are also included.

REFERENCES

Adames, Á. F., and J. M. Wallace, 2014: Three-Dimensional Structure and Evolution of the MJO and Its Relation to the Mean Flow. *Journal of the Atmospheric Sciences*, **71**, 2007–2026, https://doi.org/10.1175/JAS-D-13-0254.1.

Beniston, M., 2005: Mountain Climates and Climatic Change: An Overview of Processes Focusing on the European Alps. *Pure appl. geophys.*, **162**, 1587–1606, https://doi.org/10.1007/s00024-005-2684-9.

Bergeron, T., 1960: Problems and Methods of Rainfall Investigation Address of the Honorary Chairman of the Conference. *Geophysical Monograph Series*, H. Weickmann, Ed., American Geophysical Union, 5–30.

Bryan, G. H., and J. M. Fritsch, 2002: A Benchmark Simulation for Moist Nonhydrostatic Numerical Models. *Mon. Wea. Rev.*, **130**, 2917–2928, https://doi.org/10.1175/1520-0493(2002)130<2917:ABSFMN>2.0.CO;2.

——, R. P. Worsnop, J. K. Lundquist, and J. A. Zhang, 2017: A Simple Method for Simulating Wind Profiles in the Boundary Layer of Tropical Cyclones. *Boundary-Layer Meteorol*, **162**, 475–502, https://doi.org/10.1007/s10546-016-0207-0.

Chen, X., G. H. Bryan, J. A. Zhang, J. J. Cione, and F. D. Marks, 2021: A Framework for Simulating the Tropical-Cyclone Boundary Layer Using Large-Eddy Simulation and Its Use in Evaluating PBL Parameterizations. *Journal of the Atmospheric Sciences*, https://doi.org/10.1175/JAS-D-20-0227.1.

Chow, F., C. Schär, N. Ban, K. Lundquist, L. Schlemmer, and X. Shi, 2019: Crossing Multiple Gray Zones in the Transition from Mesoscale to Microscale Simulation over Complex Terrain. *Atmosphere*, **10**, 274, https://doi.org/10.3390/atmos10050274.

Deardorff, J. W., 1980: Stratocumulus-capped mixed layers derived from a three-dimensional model. *Boundary-Layer Meteorol*, **18**, 495–527, https://doi.org/10.1007/BF00119502.

Durran, D. R., M. O. G. Hills, and P. N. Blossey, 2015: The Dissipation of Trapped Lee Waves. Part I: Leakage of Inviscid Waves into the Stratosphere. *Journal of the Atmospheric Sciences*, **72**, 1569–1584, https://doi.org/10.1175/JAS-D-14-0238.1.

Eidhammer, T., V. Grubišić, R. Rasmussen, and K. Ikdea, 2018: Winter Precipitation Efficiency of Mountain Ranges in the Colorado Rockies Under Climate Change. *J. Geophys. Res. Atmos.*, **123**, 2573–2590, https://doi.org/10.1002/2017JD027995.

Guichard, F., and F. Couvreux, 2017: A short review of numerical cloud-resolving models. *Tellus A: Dynamic Meteorology and Oceanography*, **69**, 1373578, https://doi.org/10.1080/16000870.2017.1373578.

Hong Kong Observatory, 2012: Report on Severe Typhoon Vicente. Accessed 10 December 2022, https://www.hko.gov.hk/en/informtc/vicente/vicente.htm

Houze, R. A., 2012: Orographic effects on precipitating clouds. *Rev. Geophys.*, **50**, RG1001, https://doi.org/10.1029/2011RG000365.

Iacono, M. J., J. S. Delamere, E. J. Mlawer, M. W. Shephard, S. A. Clough, and W. D. Collins, 2008: Radiative forcing by long-lived greenhouse gases: Calculations with the AER radiative transfer models. *J. Geophys. Res.*, **113**, D13103, https://doi.org/10.1029/2008JD009944.

Ji, F., and Coauthors, 2020: Projected changes in vertical temperature profiles for Australasia. *Clim Dyn*, **55**, 2453–2468, https://doi.org/10.1007/s00382-020-05392-2.

Jing, X., B. Geerts, Y. Wang, and C. Liu, 2019: Ambient Factors Controlling the Wintertime Precipitation Distribution across Mountain Ranges in the Interior Western United States. Part II: Changes in Orographic Precipitation Distribution in a Pseudo–Global Warming Simulation. *Journal of Applied Meteorology and Climatology*, **58**, 695–715, https://doi.org/10.1175/JAMC-D-18-0173.1.

Kirshbaum, D., B. Adler, N. Kalthoff, C. Barthlott, and S. Serafin, 2018: Moist Orographic Convection: Physical Mechanisms and Links to Surface-Exchange Processes. *Atmosphere*, **9**, 80, https://doi.org/10.3390/atmos9030080.

Kirshbaum, D. J., and R. B. Smith, 2008: Temperature and moist-stability effects on midlatitude orographic precipitation. *Q.J.R. Meteorol. Soc.*, **134**, 1183–1199, https://doi.org/10.1002/qj.274.

Lin, Y.-L., R. L. Deal, and M. S. Kulie, 1998: Mechanisms of Cell Regeneration, Development, and Propagation within a Two-Dimensional Multicell Storm. *JOURNAL OF THE ATMOSPHERIC SCIENCES*, **55**, 20.

Mallen, K. J., M. T. Montgomery, and B. Wang, 2005: Reexamining the Near-Core Radial Structure of the Tropical Cyclone Primary Circulation: Implications for Vortex Resiliency. *Journal of the Atmospheric Sciences*, **62**, 408–425, https://doi.org/10.1175/JAS-3377.1.

Morrison, H., G. Thompson, and V. Tatarskii, 2009: Impact of Cloud Microphysics on the Development of Trailing Stratiform Precipitation in a Simulated Squall Line:

Comparison of One- and Two-Moment Schemes. *Monthly Weather Review*, **137**, 991–1007, https://doi.org/10.1175/2008MWR2556.1.

Muller, C., 2013: Impact of Convective Organization on the Response of Tropical Precipitation Extremes to Warming. *Journal of Climate*, **26**, 5028–5043, https://doi.org/10.1175/JCLI-D-12-00655.1.

——, and Y. Takayabu, 2020: Response of precipitation extremes to warming: what have we learned from theory and idealized cloud-resolving simulations, and what remains to be learned? *Environ. Res. Lett.*, **15**, 035001, https://doi.org/10.1088/1748-9326/ab7130.

Muller, C. J., P. A. O'Gorman, and L. E. Back, 2011: Intensification of Precipitation Extremes with Warming in a Cloud-Resolving Model. *Journal of Climate*, **24**, 2784–2800, https://doi.org/10.1175/2011JCLI3876.1.

O'Gorman, P. A., 2015: Precipitation Extremes Under Climate Change. *Curr Clim Change Rep*, **1**, 49–59, https://doi.org/10.1007/s40641-015-0009-3.

Pavelsky, T. M., S. Sobolowski, S. B. Kapnick, and J. B. Barnes, 2012: Changes in orographic precipitation patterns caused by a shift from snow to rain: OROGRAPHIC PRECIPITATION PATTERNS. *Geophys. Res. Lett.*, **39**, https://doi.org/10.1029/2012GL052741.

Rasmussen, R., and Coauthors, 2011: High-Resolution Coupled Climate Runoff Simulations of Seasonal Snowfall over Colorado: A Process Study of Current and Warmer Climate. *Journal of Climate*, **24**, 3015–3048, https://doi.org/10.1175/2010JCLI3985.1.

Schär, C., and C. Frei, 2005: Orographic Precipitation and Climate Change. *Global Change and Mountain Regions*, U.M. Huber, H.K.M. Bugmann, and M.A. Reasoner, Eds., Vol. 23 of *Advances in Global Change Research*, Springer Netherlands, 255–266.

——, ——, D. Lüthi, and H. C. Davies, 1996: Surrogate climate-change scenarios for regional climate models. *Geophys. Res. Lett.*, **23**, 669–672, https://doi.org/10.1029/96GL00265.

Shi, X., and D. R. Durran, 2014: The Response of Orographic Precipitation over Idealized Midlatitude Mountains Due to Global Increases in CO2. *Journal of Climate*, **27**, 3938–3956, https://doi.org/10.1175/JCLI-D-13-00460.1.

——, and ——, 2015: Estimating the Response of Extreme Precipitation over Midlatitude Mountains to Global Warming. *Journal of Climate*, **28**, 4246–4262, https://doi.org/10.1175/JCLI-D-14-00750.1.

——, and Y. Wang, 2022: Impacts of Cumulus Convection and Turbulence Parameterizations on the Convection-Permitting Simulation of Typhoon Precipitation. *Monthly Weather Review*, https://doi.org/10.1175/MWR-D-22-0057.1.

Siler, N., and G. Roe, 2014: How will orographic precipitation respond to surface warming? An idealized thermodynamic perspective. *Geophys. Res. Lett.*, **41**, 2606–2613, https://doi.org/10.1002/2013GL059095.

Smith, R. B., P. Schafer, D. Kirshbaum, and E. Regina, 2009: Orographic Enhancement of Precipitation inside Hurricane Dean. *Journal of Hydrometeorology*, **10**, 820–831, https://doi.org/10.1175/2008JHM1057.1.

Thompson, G., P. R. Field, R. M. Rasmussen, and W. D. Hall, 2008: Explicit Forecasts of Winter Precipitation Using an Improved Bulk Microphysics Scheme. Part II: Implementation of a New Snow Parameterization. *Monthly Weather Review*, **136**, 5095–5115, https://doi.org/10.1175/2008MWR2387.1.

Trapp, R. J., M. J. Woods, S. G. Lasher-Trapp, and M. A. Grover, 2021: Alternative Implementations of the "Pseudo-Global-Warming" Methodology for Event-Based Simulations. *JGR Atmospheres*, **126**, https://doi.org/10.1029/2021JD035017.

Wang, Y., Y. Wang, and H. Fudeyasu, 2009: The Role of Typhoon Songda (2004) in Producing Distantly Located Heavy Rainfall in Japan*. *Monthly Weather Review*, **137**, 3699–3716, https://doi.org/10.1175/2009MWR2933.1.

Supplemental Material for

Quantifying Global-Warming Response of the Orographic Precipitation in a Typhoon Environment with Large-Eddy Simulations

Jianan Chen[a] and Xiaoming Shi[a]

[a] *Division of Environment and Sustainability, Hong Kong University of Science and Technology, Hong Kong, China*

Contents of this file:

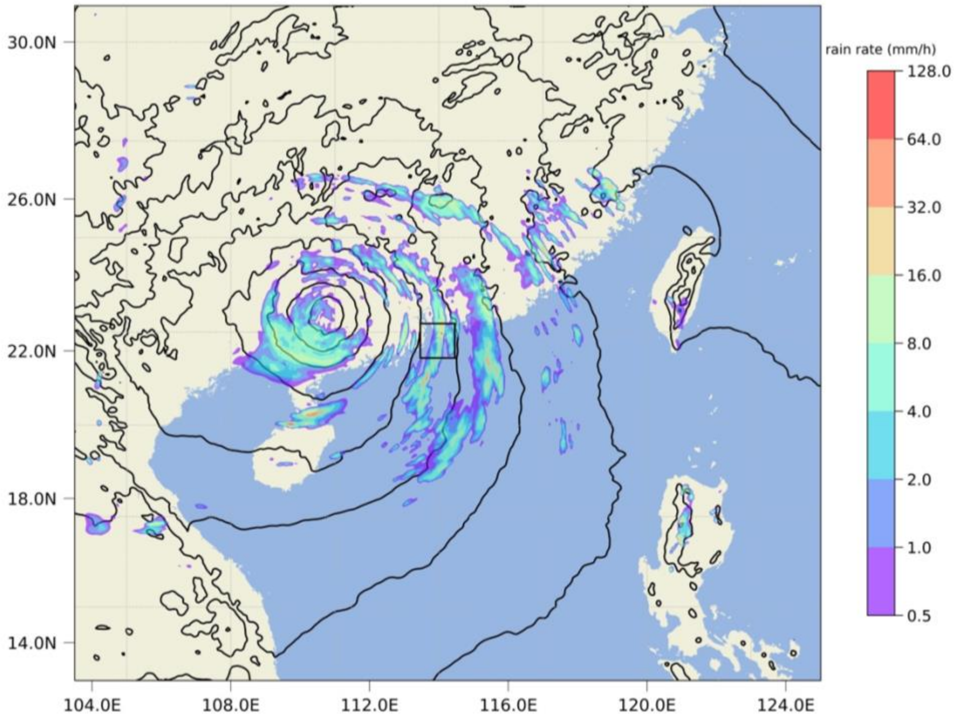

Fig. S1. Two-hour mean precipitation (color shading) and sea-level pressure (contours) between 05:00 UTC and 07:00 UTC on 24th July 2012 from the reference WRF simulation of Typhoon Vicente. Hong Kong (HK) is denoted by the black square box.

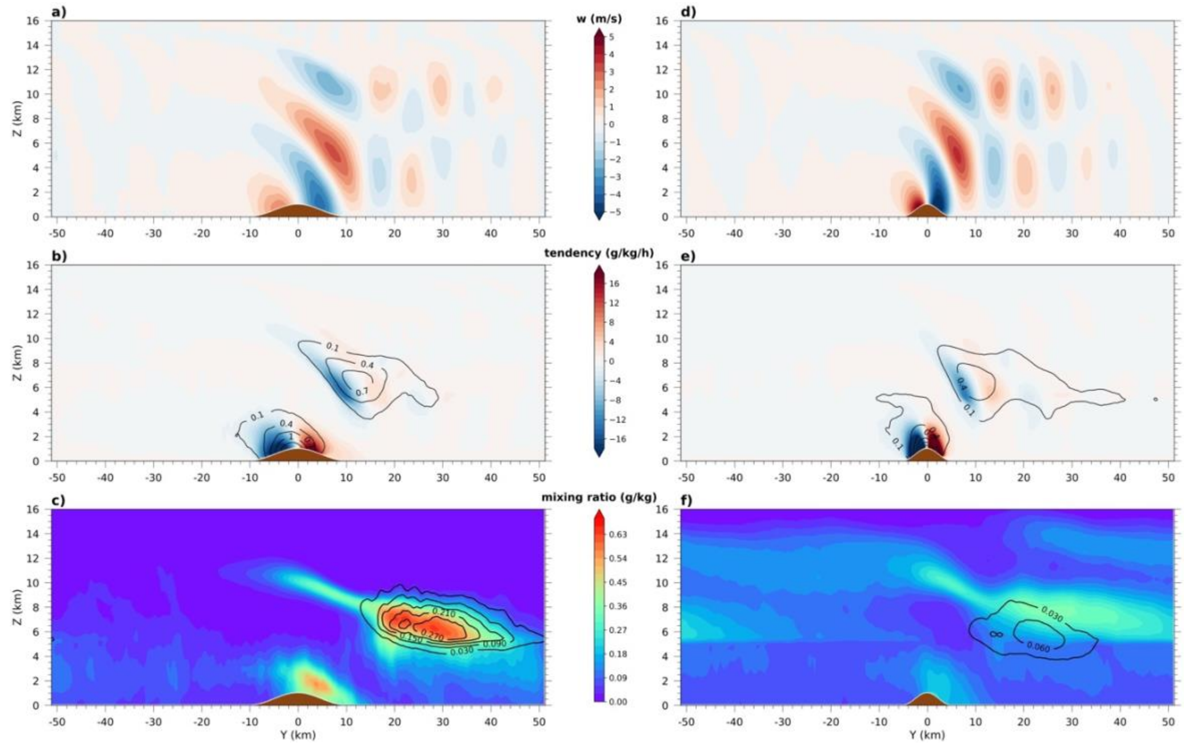

Fig. S2. same with Fig. 4, expect that a), b), c) show simulations of using the Morrison scheme, and the d), e), f) show simulations using the mountain half-width of 5 km and the Thompson scheme. In the WM simulation of the present climate, the high q_g area is collocated with the high q_p area in the Morrison scheme, whereas high q_g area is below high q_p area in the Thompson scheme (Fig. S2c and Fig. 3c). In addition, the high q_p area is located at higher altitude in the Morrison scheme (Fig. S2c and Fig. 3c). These features suggest that the transition of seeding precipitation particles from the solid phase to the liquid phase happens in an earlier stage in the Morrison scheme.

Table S1: Diagnostics of precipitation budget over the mountain (indicated by the black solid box in Fig 7): precipitation (*P*), condensation (*C*), influx to the right boundary of black solid box (F_{in}), precipitation efficiency (PE), Residual (*R*) is due to ignoring surface evaporation and storage of hydrometeors in the air.

	P(mm/hour)	*C* (mm/hour)	F_{in} (mm/hour)	PE (%)	*R/P (%)*
Present	4.53	11.79	2.06	32.73	4.79
Mid-term	4.57	11.75	2.08	33.06	5.49
Long-term	4.25	11.24	2.13	31.74	4.35

Table S2: Diagnostics of precipitation budget in the downstream area (indicated by the red solid box in Fig 7): precipitation (*P*), condensation (*C*), influx to the right boundary of red solid box (F_{in}), precipitation efficiency (PE), Residual is due to ignoring surface evaporation and storage of hydrometeors in the air.

	P (mm/hour)	*C* (mm/hour)	F_{in} (mm/hour)	PE *(%)*	*R/P (%)*
Present	2.37	5.45	5.25	22.17	0.83
Mid-term	2.92	5.51	6.00	25.35	4.27
Long-term	3.79	5.18	6.45	32.62	3.12